Multifunctional Iron Oxide Nanoflake/Graphene Composites Derived from Mechanochemical Synthesis for Enhanced Lithium Storage and Electrocatalysis

Bote Zhao,[†,‡] Yao Zheng,[∥] Fei Ye,[†,‡] Xiang Deng,[†,‡] Xiaomin Xu,[†,‡] Meilin Liu,*[,⊥] and Zongping Shao*[,†,§,#]

[†]State Key Laboratory of Materials-Oriented Chemical Engineering, [‡]College of Chemistry & Chemical Engineering, and [§]College of Energy, Nanjing Tech University, Nanjing 210009, China

[∥]School of Chemical Engineering, University of Adelaide, Adelaide, South Australia 5005, Australia

[⊥]School of Materials Science and Engineering, Center for Innovative Fuel Cell and Battery Technologies, Georgia Institute of Technology, Atlanta, Georgia 30332-0245, United States

[#]Department of Chemical Engineering, Curtin University, Perth, Western Australia 6845, Australia

S *Supporting Information*

ABSTRACT: Composites consisting of nanoparticles of iron oxides and graphene have attracted considerable attention in numerous applications; however, the synthesis methods used to achieve superior functionalities are often complex and unamenable to low-cost large-scale industrial production. Here, we report our findings in exploring a simple strategy for low-cost fabrication of multifunctional composites with enhanced properties. In particular, we have successfully prepared $FeO(OH)$ nanoflake/graphene and nano-Fe_3O_4/ graphene composites from commercially available Fe powders and graphite oxides using a simple and low-cost solid-state process, where the metallic Fe is converted to $FeO(OH)$

nanoflake and graphite oxide is reduced/exfoliated to graphene. The resultant nano-Fe_3O_4/graphene composite is multifunctional, demonstrates specific capacities of 802 and 629 mA h g^{-1}, respectively, at 1000 and 2000 mA g^{-1} as an electrode material for lithium-ion batteries (LIBs), and also displays efficient catalytic activity for both oxygen reduction reaction (ORR) and oxygen evolution reaction (OER); the nominal overpotentials are lower than those for previously reported metal-based catalysts (e.g., IrO_2, RuO_2, and Pt/C). The dramatically enhanced properties are attributed to the synergistic mechanochemical coupling effects between iron oxide and graphene introduced by the facile process, which is well suited for large-scale cost-effective fabrication.

KEYWORDS: iron oxides, graphene, nanocomposites, mechanochemical synthesis, reactive milling, lithium-ion batteries
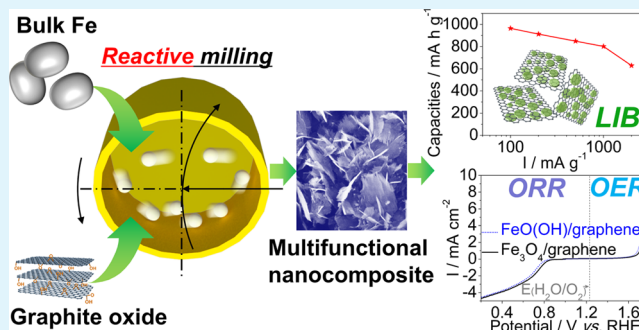
INTRODUCTION

Because of many unique and extraordinary properties of materials at the nanoscale, nanostructured materials have attracted intense attention as a vital constituent in many emerging applications.[1−4] By virtue of their nontoxicity, abundance on the earth, and many unique properties, iron oxides have been successfully used as pigments, contrast agents, and catalysts as well as in magnetic recording and energy storage and conversion.[5−8] In particular, nanosized iron oxides demonstrate significant improvement in lithium storage capacity, achieving more than twice that of the commercial graphite anode in lithium-ion batteries (LIBs). Thus, nanosized iron oxides are a promising candidate for replacing the conventional graphite anode in LIBs with enhanced safety.[7,9−13]

Furthermore, nano iron oxides have also received increasing attention as electro-catalysts for oxygen reduction reactions

(ORR) and oxygen evolution reactions (OER).[8,14,15] Being kinetically sluggish,[16] ORR and OER often become the rate-limiting step of the chemical and energy transformation processes in metal−air batteries, fuel cells, and water splitting. To date, the most efficient catalysts for ORR and OER are still precious-metal-based catalysts such as Pt-based catalysts (e.g., Pt/C) for ORR and RuO_2 (and IrO_2) for OER. Although various Co-based oxide catalysts have been studied to replace the precious-metal-based catalysts,[17−19] they are still relatively expensive. Thus, cheap and environmentally friendly nanosized iron oxides are better choice.
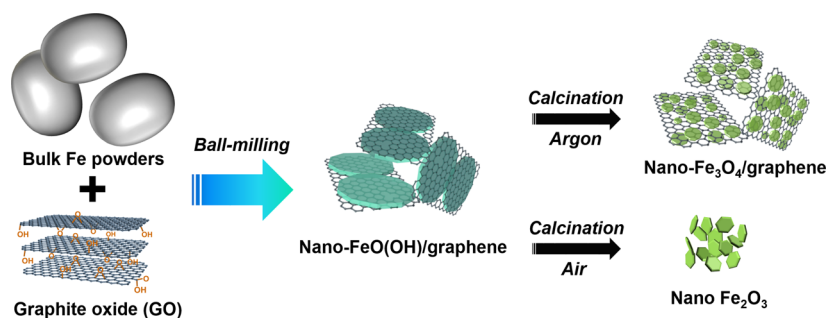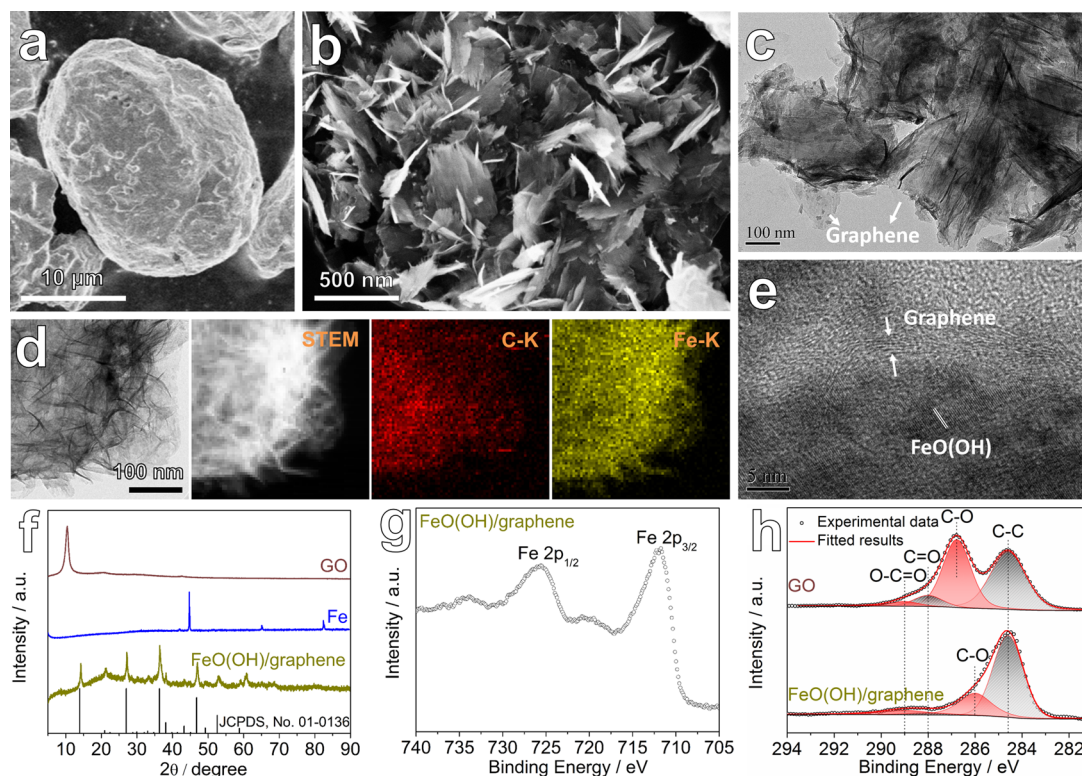
Figure 1. Schematic illustration of the preparation of nanocomposites consisting of iron oxides and graphene by a reactive solid-state milling process.

Figure 2. (a) Field-emission SEM (FE-SEM) image of bulk Fe. (b) FE-SEM image, (c) TEM image, (d) TEM image of FeO(OH)/graphene composite prepared via ball milling from Fe and GO, and the corresponding STEM image and EDX elemental distribution of C and Fe. (e) HR-TEM image of FeO(OH)/graphene composite. (f) XRD patterns of GO, bulk Fe, and FeO(OH)/graphene composite. The XRD intensities of Fe and FeO(OH)/graphene samples are multiplied by a factor of 2 and 10, respectively. (g) XPS spectrum of Fe 2p in FeO(OH)/graphene composite. (h) XPS spectra of C 1s in GO and FeO(OH)/graphene composite.

However, nanosized iron oxides usually suffer from uncontrollable agglomeration and growth during synthesis, which greatly degrade their performance. Additionally, iron oxides have a relatively low electrical conductivity that further limits their potential in lithium storage and electro-catalysis. To overcome these obstacles, synthesis of nanosized iron oxides on a conductive support has been well-recognized as an effective strategy. To date, a wide variety of solution-based processes have been successfully used to synthesize nanosized iron-based oxides on graphene, such as hydrothermal/solvothermal synthesis,[14,20−22] microwave-assisted sol−gel process,[23] chemical deposition under CO_2,[24] and other solution methods with the assistance of atomic layer deposition,[25] plasma,[26] and infrared irradiation.[27] The highlights for anchoring nanosized iron oxides on graphene can be briefly summarized as follows: (1) The large surface area of graphene offers rich sites for uniformly anchoring oxides. (2) Oxygen-containing functional groups on graphene could introduce strong interaction with iron oxides. (3) Graphene is not only a support but also a conductive medium for efficient current collection and even an active material. (4) The as-formed nanosized iron oxides could also suppress the restacking of graphene. (5) The flexibility of graphene can effectively accommodate the volume variation of iron oxides during charge/discharge cycling. Thus, the significantly enhanced properties of the nano iron oxide/graphene composites are attributed to the synergistic effects between the two components. For instance, the iron oxide/graphene nanostructured anodes for LIBs, prepared by a microwave-assisted sol−gel process in benzyl alcohol, exhibited a specific capacity of 500 mA h g^{-1} at a current density of 1600 mA g^{-1}.[23] Similarly, Fe_3O_4 nanoparticles on 3D N-doped graphene were successfully synthesized as an efficient catalyst for ORR by a combined hydrothermal, freeze-drying, and thermal treatment.[14] The composite showed high electro-

catalytic activity, including a high kinetic current density and an electron transfer number of ~4.

Despite the tremendous progress achieved in the synthesis of iron oxide/graphene for various applications, these liquid-state synthesis methods require additional chemicals or harsh conditions or involve complex processes. Furthermore, graphene or graphene oxide was used as starting material, which is relatively expensive. A solid-state method is still the most attractive choice for large-scale industrial applications. Recently, we have examined a solid-state ball milling process for the preparation of SnO_2/graphene nanocomposites, which showed outstanding performance as an anode for LIB.[28]

In this study, we extended this promising strategy to other functional materials, resulting in a unique nanoflake-micro-structure-based composite for multifunctional application in enhanced energy storage and conversion. As schematically shown in Figure 1, nano iron oxide/graphene composites as multifunctional materials for lithium storage, ORR, and OER can be prepared on a large scale from commercially available bulk Fe and graphite oxide (GO). The mechanochemical interactions between iron oxide and graphene are vital to the formation of nanocomposites for LIB electrodes and for bifunctional electrocatalysts with favorable electrocatalytic activity for ORR and OER in metal–air batteries. The excellent electrochemical performance of Fe_3O_4/graphene nanocomposite as anode for LIBs is comparable to that of recently reported advanced iron oxide/graphene nanocomposite prepared by solution methods at a much lower cost. They can also be used to replace expensive precious-metal-based catalysts for ORR and OER in metal–air batteries. Additionally, the electrocatalytic property of FeO(OH)/graphene for ORR and OER was rarely reported. This simple and low-cost fabrication process is vital to commercialization of multifunctional nanocomposite electrodes for next-generation LIBs and metal–air batteries.

■ RESULTS AND DISCUSSION

Ball milling is an efficient solid-state method for grinding various materials into fine powders. The milling process in which bulk materials are ground into fine powders through only a physical process is called "non-reactive grinding".[29] The raw bulk Fe powders used in this study were irregular in shape with particle sizes of 10–30 μm (Figures S1 and 2a). Figure 2a shows a typical field-emission scanning electron microscopy (FE-SEM) image of a single metallic Fe particle, which appeared to be dense. When milled without addition of GO under Ar atmosphere (a non-reactive grinding" process), bulk Fe powders were ground to micrometer-sized plates; the average particle size was reduced to <10 μm (Figure S2). When chemical reactions take place simultaneously during the milling, it is termed "reactive grinding",[29] also known as mechanochemical synthesis.[30] The grinding process with Fe particles and GO is a typical reactive grinding process, as schematically shown in Figure 1. The repeated fracturing and rewelding of reactant powders during the mechanical process promotes intimate contact between metallic Fe and GO; at the same time, GO offered rich reaction sites for the formation of nanosized iron-based oxide (i.e., FeO(OH) nanoflakes) on the surface of graphene. GO was reduced by metallic iron and exfoliated simultaneously to form graphene. Fe_3O_4/graphene nanocomposite and independent nano Fe_2O_3 could be easily obtained after calcination of FeO(OH)/graphene under Ar and air, respectively. After grinding with GO, the Fe particles

were transformed to nanostructured flakes (Figure 2b). Additionally, the as-obtained products have much smaller particle size than those obtained in the absence of GO, suggesting that the GO played a very important role in creating the nanostructures. To reveal the detailed microstructures of the products from ball milling of metallic Fe and GO, the samples were characterized using transmission electron microscopy (TEM) (Figure 2c–e). As shown in Figure 2c, transparent and thin graphene sheets were observed, and their surfaces were almost covered by flake-like Fe-based compounds, indicating that the bulk Fe powders were successfully transformed to nanostructured composites by ball milling with GO. During the TEM analysis, minor needle-like and spindle-like Fe-based compounds were also observed. The transparent and thin graphene sheets (Figure 2c) suggest that the graphite oxides were exfoliated during the ball milling process. The Fe-based compounds covering the surface of graphene sheets also prevented the graphene from restacking. As seen in Figure 2d, the EDX mapping of the as-prepared composite indicates that the Fe and C elements were relatively homogeneously distributed, confirming that the graphene sheets were covered by flake-like Fe-based compounds. As shown in a HR-TEM image of the composite (Figure 2e), graphene layers are observed, confirming that the graphite oxides were successfully exfoliated under the physical and chemical processes during the ball milling.

We also performed X-ray diffraction (XRD) and X-ray photoelectron spectroscopy (XPS) to further understand the reaction between metallic Fe and GO during the ball milling process. As seen in the typical XRD patterns (Figure 2f), a characteristic peak located at 2θ of 10.4° is observed for the GO raw material, which is consistent with the other reports;[31,32] three strong peaks at 2θ = 44.7, 65.1, and 82.4°, corresponding to (110), (200), and (211) lattice planes of metallic-phase Fe (Powder Diffraction File (PDF) 87-0722, International Centre for Diffraction Data, 2002), are present for the bulk Fe powders. After grinding, the characteristic peaks corresponding to the GO and metallic Fe phases all disappeared, indicating that the redox reaction happened and was completed under the mechanical process. The XRD pattern for the composite was assigned to lepidocrocite FeO(OH) (another chemical formula: $Fe_2O_3 \cdot H_2O$) (PDF 01-0136, International Centre for Diffraction Data, 2002), suggesting that the initial metallic Fe was successfully oxidized by GO during the grinding. The XPS analysis of the samples was conducted from 0 to 1000 eV (Figure S3), which confirmed the presence of Fe, O, and C elements in the as-prepared composite. Figure 2g displays a high-resolution XPS spectrum of Fe 2p in FeO(OH)/graphene composite, in which the two main peaks centered at 725.6 (Fe $2p_{1/2}$) and 711.9 (Fe $2p_{3/2}$) eV were observed, confirming the formation of FeO(OH).[33] The high-resolution XPS spectra of C 1s in initial GO and the as-prepared FeO(OH)/graphene composite were then analyzed to confirm that the successful reduction of GO by metallic Fe during the ball milling. As shown in Figure 2h, for the initial GO, the C 1s peak could be deconvoluted into four peaks associated with C–C-type carbon (284.6 eV), C–O-type carbon (286.8 eV, including C–OH and C–O–C (epoxide groups)), C=O-type carbon (288.0 eV), and small amounts of O–C=O-type carbon (289.0 eV).[34,35] After grinding with metallic Fe, the intensity of oxygen-containing functional groups, especially for C–O and C=O, significantly decreased and C–C bond intensity at 284.6 eV increased, confirming that GO was successfully reduced by
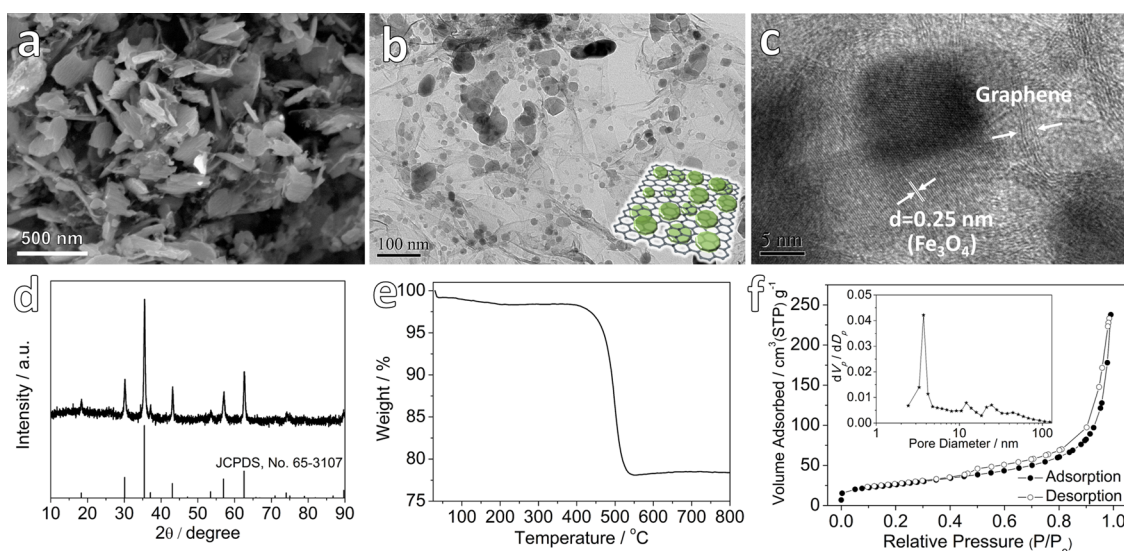
Figure 3. (a) FE-SEM image, (b) TEM image, (c) HR-TEM image, (d) XRD pattern, (e) thermogravimetric analysis profile, and (f) nitrogen adsorption−desorption isotherm of Fe_3O_4/graphene nanocomposite. The inset in f is the corresponding BJH pore size distribution plot.

metallic Fe and that the as-obtained thin carbon sheets were graphene sheets instead of graphene oxide sheets. The shift of C−O after grinding was mainly due to the reduction of epoxide groups in C−O groups.

Additionally, graphene (instead of GO) was used as raw material to be ground with bulk Fe powders at a weight ratio of 1:1 under Ar atmosphere to further investigate the function of GO in the ball milling process. After milling for 8 h 20 min, the morphology of the as-obtained composite appeared to be very different from the sample using Fe and GO as raw materials. FE-SEM images (Figure S4) demonstrated that there was almost no flake in the composite. Instead, particles with sizes from dozens of nanometers to several hundreds of nanometers were observed. Some particles appeared to be independent. TEM observation (Figure S5) further confirmed that almost no nanoflake formed using Fe and graphene as raw materials. Some individual large particles were still observed. There were also some nanoparticles attached to graphene (Figure S5b) probably caused by the presence of some residual oxygen-containing groups in the graphene. These results suggest that the oxygen-containing groups in GO play an important role in promoting a redox reaction with metallic Fe, which facilitates the formation of a strong bond between the as-formed Fe-based oxide and graphene leading to nano-FeO(OH)/graphene composite. In comparison with the results achieved by grinding Fe powders alone, it appears that the GO also acted as a grinding medium in the ball milling process to reduce the size of Fe powders.

To obtain Fe_3O_4/graphene composite, the as-obtained FeO(OH)/graphene composite was calcined at 600 °C in Ar for 2 h. The XRD pattern (Figure 3d) indicates that the as-calcined product has a pure Fe_3O_4 phase (PDF 65-3107, International Centre for Diffraction Data, 2002). The typical FE-SEM image is shown in Figure 3a. The initial FeO(OH) nanoflakes (Figure 2b) were transformed to smaller Fe_3O_4 nanoflakes because of the decomposition of FeO(OH) and the reaction with graphene. Figure 3b shows the corresponding TEM images. Most of the as-obtained Fe_3O_4 appear to be nanoflakes, and some very small ones could be recognized as nanoparticles (Figures 3b and S6), even though the sizes of Fe_3O_4 were not very uniform. (Lots of them were <30 nm,

Figure S7.) Figure 3c shows a HR-TEM image, in which clear graphene layers and the periodic lattice fringe corresponding to Fe_3O_4 phase are observable. The interplanar distance of 0.25 nm was assigned to the (311) plane of Fe_3O_4 phase. Thermogravimetric analysis (TGA) was carried out in air to quantify the amount of graphene in the composite (Figure 3e). The weight loss over the temperature range below 200 °C could be attributed to the loss of the absorbed moisture. Most of the weight loss of the composite occurring within the temperature range of 400−550 °C is attributed mainly to combustion of graphene in air. The graphene content was calculated to be 23 wt % on the basis of the weight loss upon graphene combustion and the assumption that Fe_3O_4 was fully oxidized to Fe_2O_3. As shown in Figure 3f, the nitrogen adsorption−desorption isotherm for the as-prepared nano-Fe_3O_4/graphene composite has a distinct hysteresis loop when the relative pressure is >0.4, suggesting the presence of a porous structure. The corresponding pore size distribution (Figure 3f, inset), calculated by the Barret−Joyner−Halenda (BJH) method using the desorption branch, indicates the existence of mesopores. The BET specific surface area was 92.2 $m^2\ g^{-1}$. The FeO(OH)/graphene composite was also calcined under air to burn the graphene to obtain independent nanosized iron oxide (Figure S8). The morphology was somewhat different from that of the FeO(OH) nanoflake attached to the graphene because of the decomposition of FeO(OH) during calcination, but the nanoflake morphology still remains. In the absence of graphene, the nanosized Fe_2O_3 were somewhat agglomerated and partially sintered during the calcination. The HR-TEM images of the nanoflakes indicated that they were Fe_2O_3 phase. Thus, the nanosized Fe_2O_3 and Fe_3O_4/graphene were successfully prepared through a reactive solid-state milling process with a subsequent heat treatment, which can be readily scaled up for industrial production.

When iron oxides (alone) were used as an anode for LIBs, the performance was very poor, primarily because of the large volume variation during the discharge/charge cycling and the formation of insulating Li_2O during discharge. The use of nano iron oxide/graphene composite electrodes has the potential to enhance the cycling performance significantly.[23−26] To evaluate this potential, the as-prepared Fe_3O_4/graphene nanocomposite
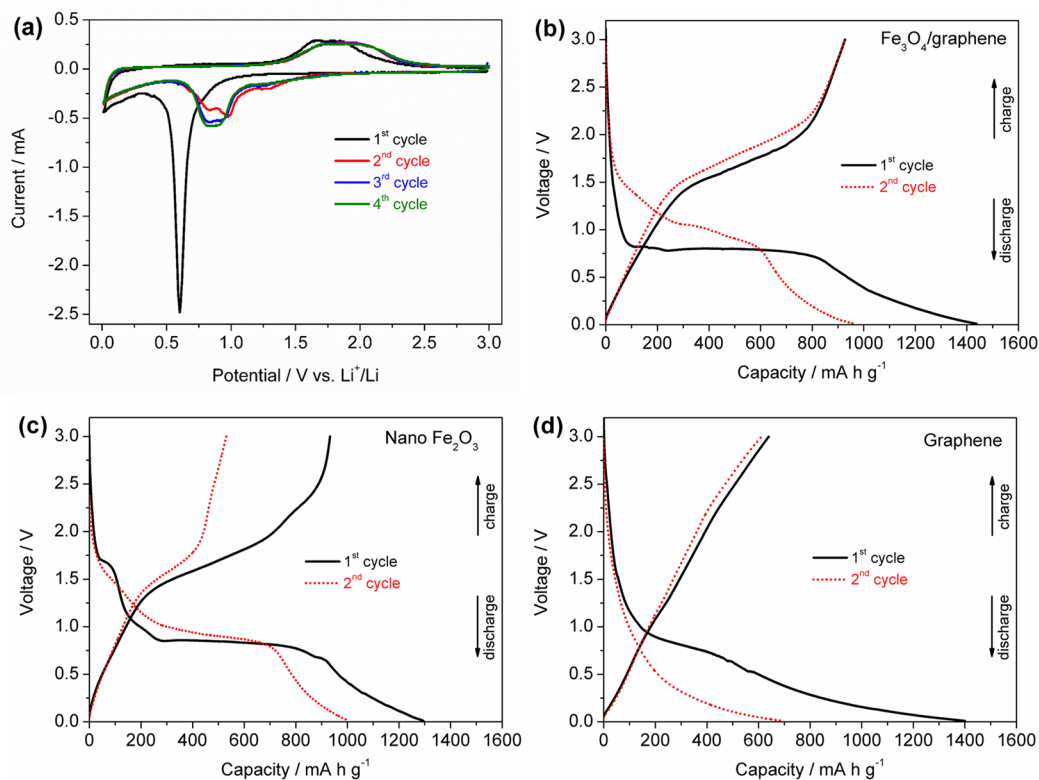
Figure 4. (a) Cyclic voltammograms of the Fe_3O_4/graphene nanocomposite between 3.0 and 0.01 V at a sweep rate of 0.1 mV s^{-1}. (b−d) First and second discharge−charge curves of the cells with (b) Fe_3O_4/graphene nanocomposite, (c) nano Fe_2O_3, and (d) graphene (from Fe_3O_4/graphene nanocomposite) electrodes at 100 mA g^{-1} between 0.01 and 3.0 V.

was used as the working electrode in a coin cell with metallic lithium foil as the counter electrode. Shown in Figure 4a are some typical cyclic voltammograms acquired in the potential range of 3.0−0.01 V at a sweep rate of 0.1 mV s^{-1}. In the first cycle, we observed a sharp cathodic peak centered at approximately 0.6 V, which could be attributed to the reduction of Fe^{3+}/Fe^{2+} to Fe^0, as well as the irreversible reaction related to the decomposition of the electrolyte. The subsequent anodic peaks at approximately 1.66 and 1.86 V were usually ascribed to the reversible oxidation of Fe^0 to Fe^{3+}/Fe^{2+}.[24,36] However, the definite conversion mechanism is not very clear because the delithiated product from initial Fe^{3+} was reported to be Fe^{2+} from in situ TEM analysis.[37] After the first cycle, the cyclic voltammogram curves showed pair of redox peaks at ∼0.86 and 1.7−2.0 V for reversible conversion reaction and tended to be stable in subsequent cycles, which is in good agreement with the results in the literature.[24,36,38] Figure 4b shows the first and second discharge−charge curves of the cell with Fe_3O_4/graphene electrode at a current density of 100 mA g^{-1} in the potential range of 0.01−3.0 V. The initial discharge capacity of 1438 mA h g^{-1} was achieved, whereas the subsequent first charge capacity was 928 mA h g^{-1}. The Coulombic efficiency for the first cycle was approximately 64.5%. The irreversible capacity loss was mainly due to the irreversible formation of a solid−electrolyte interface (SEI) layer and to the reaction of lithium ions with residual oxygen-containing functional groups on graphene sheets, which are common for the previously reported metal oxide/graphene anode materials.[25,27] In the second cycle, the Coulombic efficiency increased to 96.3%, and the second charge capacity was almost the same as the initial

charge capacity, indicating its reversible lithium storage property. As a comparison, the electrochemical performance of the as-prepared Fe_2O_3 nanoflakes alone was also studied under similar conditions; the first and second discharge−charge curves are shown in Figure 4c. The first charge capacity appeared to be similar to that of the Fe_3O_4/graphene nanocomposite electrode. However, the second charge capacity of the Fe_2O_3 electrode decreased rapidly to 531 mA h g^{-1}, which is much lower than that of the Fe_3O_4/graphene nanocomposite electrode, confirming the important role of the graphene in the composite electrode for lithium storage. To further understand the role of the graphene in the nanocomposite, the Fe_3O_4/graphene nanocomposite was treated in HCl solution to dissolve the Fe_3O_4 to obtain bare graphene. The lithium storage property of graphene (alone) was also investigated under the same testing conditions; the results are shown in Figure 4d. In the absence of Fe_3O_4, the long voltage plateau at around 0.8 V in the first discharge was displaced by a short sloped voltage plateau, and the short plateau was mainly due to the formation of SEI layer. The subsequent charge curve appeared to be a straight line with a reversible capacity of 639 mA h g^{-1}, suggesting that the graphene in the nanocomposite also acts as an active material for lithium storage. According to the second cycle of graphene (obtained from Fe_3O_4/graphene nanocomposite), Fe_2O_3 nanoflakes (the theoretical capacity is slightly higher than that of Fe_3O_4), and Fe_3O_4/graphene nanocomposite electrodes, the second charge capacity of the Fe_3O_4/graphene nanocomposite was much higher than that of the graphene or the Fe_2O_3 nanoflakes. It suggests that a positive synergistic effect was introduced in the Fe_3O_4/graphene
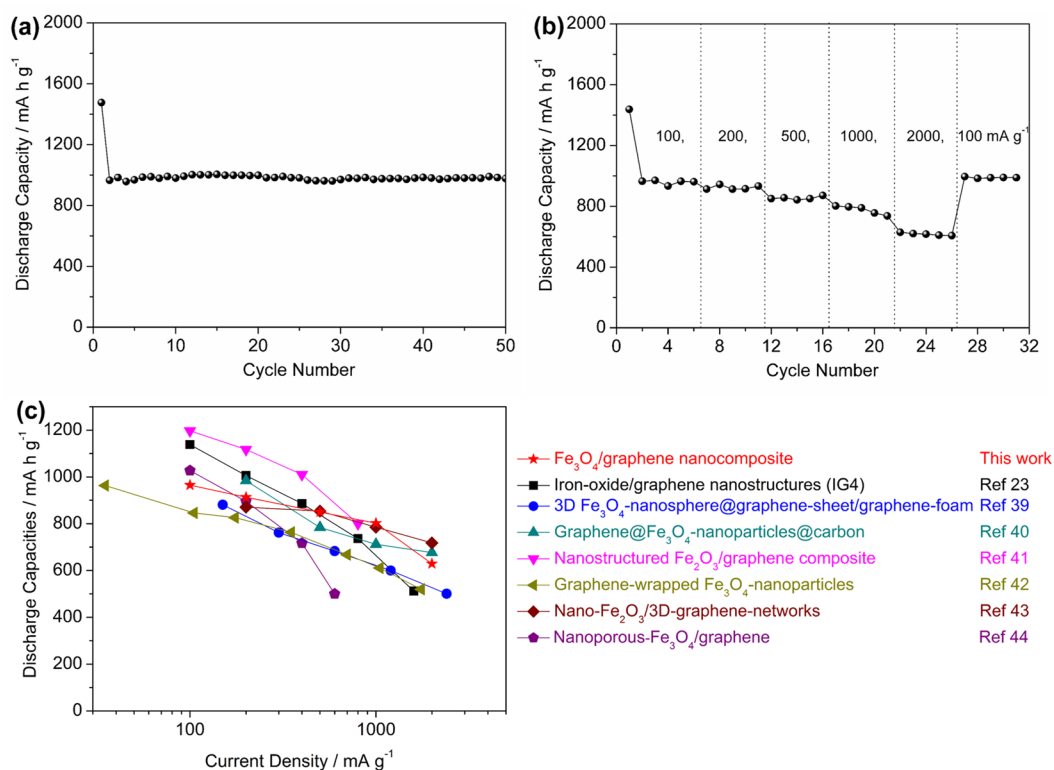
Figure 5. (a) Cycling performance of the cell with the Fe_3O_4/graphene nanocomposite electrode at 100 mA g^{-1} between 0.01 and 3.0 V. (b) Cycling performance of the cell with the Fe_3O_4/graphene electrode at various current densities of 100, 200, 500, 1000, and 2000 mA g^{-1} between 0.01 and 3.0 V. (c) Comparison of discharge capacities at different current densities for the Fe_3O_4/graphene nanocomposite electrode with other recently reported advanced iron oxide/graphene composite electrodes.

nanocomposite by physical and chemical interaction during the reactive grinding.

To further investigate the electrochemical stability of the Fe_3O_4/graphene nanocomposite, the cycling performance was tested at 100 mA g^{-1} in the potential range of 0.01−3.0 V, and the result is shown in Figure 5a. After the initial cycle, the performance of Fe_3O_4/graphene composite electrode was very stable, and a specific capacity of 977 mA h g^{-1} was achieved even after 50 cycles, indicating a reversible conversion reaction for the as-prepared Fe_3O_4/graphene nanocomposite. The value (977 mA h g^{-1}) is much higher than the theoretical capacity of commercial graphite anode (372 mA h g^{-1}). Figure 5b shows cycling performance of the cell with an Fe_3O_4/graphene electrode at various current densities (100−2000 mA g^{-1}). The electrode delivered capacities of 913, 850, and 802 mA h g^{-1} at current densities of 200, 500, and 1000 mA g^{-1}, respectively. At a current density as high as 2000 mA g^{-1}, a specific capacity of 629 mA h g^{-1} was still achieved. More importantly, by decreasing the current density back to 100 mA g^{-1} after the cycling test at various current densities of 100−2000 mA g^{-1}, the specific capacity of the Fe_3O_4/graphene electrode could recover to the initial value, confirming the reversible conversion reaction and excellent cycling stability. The excellent electrochemical performance is attributed to the nanostructuring of Fe_3O_4 that could accommodate volume variation during discharge/charge processes, the presence of graphene that provides good electron transport path, the large surface area that increases the electrolyte/electrode contact area, and the as-formed bonds between Fe_3O_4 and graphene introduced by redox reaction during ball milling process that could prevent the Fe_3O_4 from peeling off from the graphene sheets. The rate

performance of the Fe_3O_4/graphene nanocomposite electrode was comparative with that of the recently reported advanced nano iron oxide/graphene composite electrodes prepared using solution-based synthesis methods (Figure 5c), including iron oxide/graphene nanostructures (IG4),[23] 3D Fe_3O_4-nanosphere@graphene-sheet/graphene-foam,[39] graphene@Fe_3O_4-nanoparticles@carbon,[40] nanostructured Fe_2O_3/graphene composite,[41] graphene-wrapped Fe_3O_4 nanoparticles,[42] nano-Fe_2O_3/3D-graphene networks,[43] and a nanoporous-Fe_3O_4/graphene hybrid.[44] Additionally, the preparation procedures and the chemicals used for synthesis of these advanced electrodes are also summarized in Table S1. Obviously, our reactive solid-state (mechanochemical) strategy for preparing Fe_3O_4/graphene nanocomposite is facile, low-cost, and environmentally friendly. However, compared to the liquid-state synthesis method, the microstructure of the as-prepared Fe_3O_4/graphene nanocomposite derived from the mechano-chemical synthesis appeared to be not very uniform. Decreasing the heating rate (from the rate of 5 °C min^{-1} used for the preparation of the Fe_3O_4/graphene nanocomposite) during the calcination process may help to obtain more uniform particles, which could further improve the electrochemical performance. Additionally, other low-cost and green chemicals could be further introduced into the mechanochemical synthesis process, which we expect to result in more unique and uniform microstructures.

To assess the electrocatalytic activity for ORR and OER of the as-prepared nano-FeO(OH)/graphene and nano-Fe_3O_4/graphene composites, the catalysts were loaded onto glassy-carbon electrodes for rotating-disk electrode (RDE) measurements in an alkaline solution (O$_2$-saturated 0.1 M KOH).
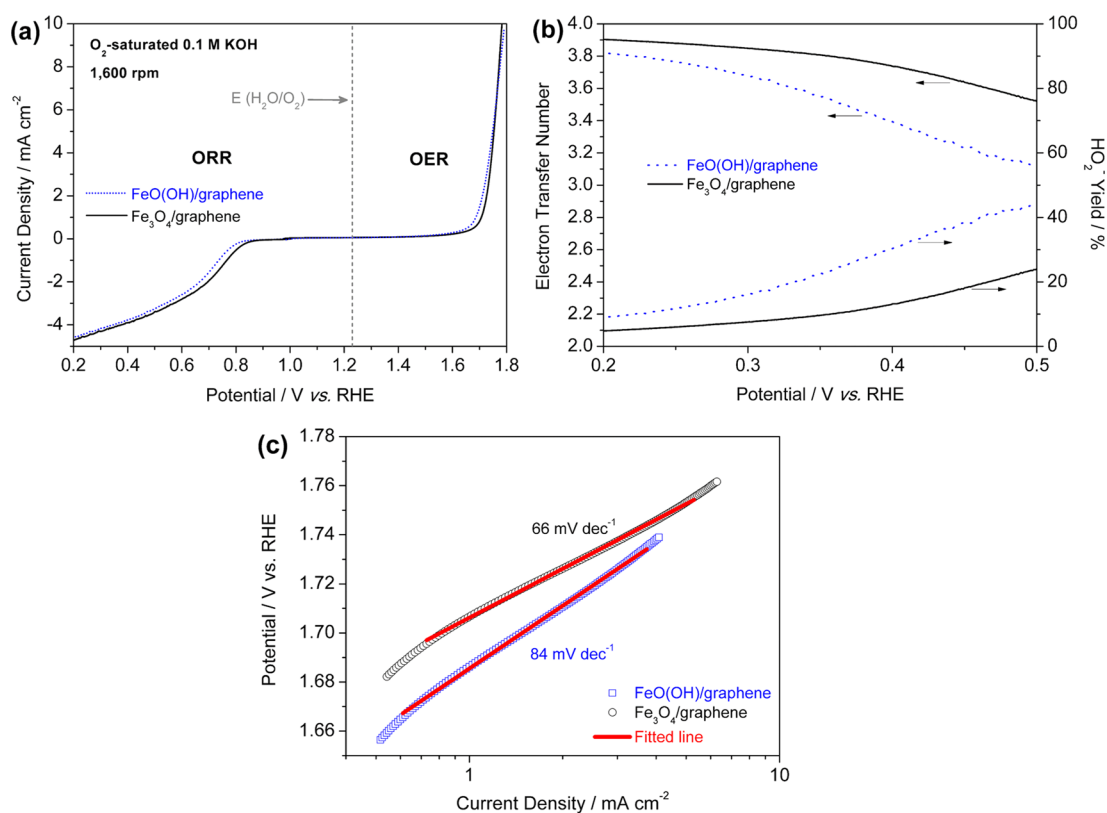
Figure 6. (a) Oxygen electrode activities of nanostructured FeO(OH)/graphene and Fe_3O_4/graphene composites within the ORR and OER potential window in O_2-saturated 0.1 M KOH solution at a rotating speed of 1600 rpm. (b) Corresponding electron transfer number and extent of HO_2^- yield at various potentials of FeO(OH)/graphene and Fe_3O_4/graphene nanocomposites derived from the RRDE data in Figure S11. (c) Tafel plots derived from Figure 6a within the OER potential window; adjusted R^2 of fitted line > 0.999.

Figure 6a shows the typical linear sweep voltammograms (LSVs) of the composites in both ORR and OER zones with an RDE rotating speed of 1600 rpm. Both nano-FeO(OH)/graphene and nano-Fe_3O_4/graphene electrodes demonstrated favorable ORR and OER electrocatalytic activities as bifunctional electrocatalysts. Specifically, in terms of ORR property, Fe_3O_4/graphene electrode shows both higher ORR current density and more positive ORR onset potential than those of the FeO(OH)/graphene electrode, suggesting an enhanced ORR catalytic activity after the calcination. These two ORR polarization curves appeared to be similar to that reported for 3D N-doped graphene-aerogel-supported Fe_3O_4 nanoparticles with a possible direct four-electron transfer pathway but appear to be different from that on Fe_3O_4 nanoparticles supported on N-doped carbon black and N-doped graphene sheet, which shows obvious two-step reaction pathways.[14] To further investigate the ORR mechanism and quantify the ORR reaction pathways on these two active nonprecious-metal hybrids, a series of ORR polarization curves at different rotating speeds (400–2400 rpm, Figure S9) were measured for Koutecky–Levich (K–L) plot fitting. On the basis of the slopes of K–L plots (Figure S10), the electron transfer numbers (n) were calculated to be 3.54 and 3.68 at 0.48 V versus reversible hydrogen electrode (RHE) for FeO(OH)/graphene and Fe_3O_4/graphene composites, respectively. The corresponding kinetic current densities are 9.65 and 10.33 mA cm^{-2}, respectively, both indicating a more favorable ORR activity on nano-Fe_3O_4/graphene catalyst. Additionally, a rotating ring-disk electrode (RRDE) technique was also applied to quantify the ORR electron transfer pathway by directly monitoring the

intermediate HO_2^- generation rates on these two electrodes during the ORR process (Figure S11). As shown in Figure 6b, the Fe_3O_4/graphene electrode exhibited lower HO_2^- yield (i.e., higher electron transfer numbers) compared to that of FeO(OH)/graphene sample under all testing potentials. The former also possesses an electron transfer number of 3.90–3.52 within the potential range of 0.20–0.50 V versus RHE, indicating a near-four-electron reaction pathway as an efficient catalyst for ORR in an alkaline solution.

For the OER catalytic activity, the FeO(OH)/graphene composite displayed a slightly lower onset potential compared to that of Fe_3O_4/graphene composite (Figure 6a). However, as shown in Figure 6c, the Tafel slope of the Fe_3O_4/graphene composite (66 mV dec^{-1}) was lower than that of FeO(OH)/graphene sample (84 mV dec^{-1}); therefore, Fe_3O_4/graphene nanocomposite was a more efficient electrocatalyst at higher current densities. Specifically, the potential of Fe_3O_4/graphene sample at current density of 10 mA cm^{-2}, which is a metric related to solar fuel synthesis,[45] was lower compared to that of FeO(OH)/graphene sample. The OER and ORR activity was further compared with that recently reported for IrO_2, RuO_2, Pt/C, Ni_xO_y/N-carbon, Mn_xO_y/N-carbon, and Co_xO_y/N-carbon (Table 1).[46] The overvoltage between ORR and OER is recognized to be a significantly important parameter for assessing the bifunctional activity.[46] The ORR activity was compared on the basis of the potential at −1 mA cm^{-2}. Obviously, the Fe_3O_4/graphene nanocomposite demonstrated lower overvoltage between ORR and OER compared to that of the precious-metal-based catalysts (i.e., IrO_2, RuO_2, and Pt/C).[46] The overvoltage of Fe_3O_4/graphene nanocomposite is

Table 1. Bifunctional Activity of Nanostructured FeO(OH)/graphene and Fe₃O₄/graphene Composites and That Reported for IrO₂, RuO₂, Pt/C, NiₓOᵧ/N-carbon, MnₓOᵧ/N-carbon, and CoₓOᵧ/N-carbon for ORR and OER

catalyst	E_{ORR} (V)[a]	E_{OER} (V)[b]	ΔE (V)[c]
Fe₃O₄/graphene	0.86	1.78	0.92
FeO(OH)/graphene	0.83	1.79	0.96
IrO₂[46]	0.38	1.70	1.32
RuO₂[46]	0.54	1.64	1.10
Pt/C[46]	0.96	1.90	0.94
NiₓOᵧ/N-carbon[46]	0.71	1.64	0.93
MnₓOᵧ/N-carbon[46]	0.81	1.68	0.87
CoₓOᵧ/N-carbon[46]	0.80	1.66	0.86

[a]At −1 mA cm⁻². [b]At 10 mA cm⁻² [c]$\Delta E = E_{ORR} - E_{OER}$.

lower than that of NiₓOᵧ/N-carbon and higher compared to that of MnₓOᵧ/N-carbon and CoₓOᵧ/N-carbon. However, the synthesis method in this work is definitely facile and cost-effective, and iron is by mass the more common element on the earth. Thus, the FeO(OH)/graphene and Fe₃O₄/graphene nanocomposites prepared via the reactive solid-state milling strategy using bulk Fe and GO as raw materials, especially for nano-Fe₃O₄/graphene composite, delivered an efficient electrocatalytic activity for both ORR and OER, indicating that both these nanocomposites are potential cost-effective bifunctional electrocatalysts in alkaline solution. Further improvement in the electrocatalytic activity may be achieved by doping nitrogen (and/or other element) in graphene, optimizing the ratio of Fe₃O₄ to graphene and introducing other metal to form bi/multimetal oxide, etc.

CONCLUSIONS

FeO(OH) nanoflake was successfully prepared and layered on graphene to form a nanocomposite via a one-step reactive solid-state strategy using low-cost bulk Fe and graphite oxide as raw materials. Nano Fe₃O₄/graphene and Fe₂O₃ could be easily obtained after further calcination under Ar and air, respectively. The as-prepared nano-Fe₃O₄/graphene composite is multifunctional, delivering high capacity, excellent cycling, and rate performance as electrode for LIBs, and exhibits an efficient catalytic activity for both ORR and OER. The facile synthesis method, low-cost raw materials, and good properties make the as-prepared nano-Fe₃O₄/graphene composite a competitive candidate for electrode or catalyst for new energy systems. The as-obtained nano Fe₂O₃ is also expected to have potential application in polishing, pigments, and magnetic recording. Additionally, bare graphene has also been obtained by the solid-state reduction and exfoliation from graphite oxides. This study offers a new avenue to large-scale commercial application of multifunctional nano iron oxides and their graphene composites.

EXPERIMENTAL SECTION

Materials Synthesis. Graphite oxide (GO) was prepared from natural graphite using a modified Hummers method[47] and then dried at room temperature. In a typical reactive ball milling process, 0.8 g of GO chips and 0.8 g of Fe powders (≥98.0%) were added into a 80 mL stainless-steel grinding bowl and ground in deionized water media under Ar using a Pulverisette-6 planetary mill at a rotational speed of 400 rpm for 8 h 20 min, with cycles of 20 min grinding and 10 min break. The grinding balls were zirconium dioxide balls (5 mm in diameter) with a ball to powder (GO + metal) weight ratio of 34:1−40:1. After being dried at room temperature, the sample was calcined

at 600 °C for 2 h under Ar to obtain nano-Fe₃O₄/graphene or calcined at 500 °C for 2 h under air to obtain nano-Fe₂O₃. In contrast, for the experiment of ball milling metallic Fe and graphene, the graphene was a commercial product (XF001H, Nanjing XFNANO Materials Tech Co., Ltd.) that was prepared by modified Hummers method and reduced by a chemical reducing agent. To obtain bare graphene for investigating its lithium-storage property, the nano-Fe₃O₄/graphene was refluxed in a concentrated HCl solution at 80 °C for more than 3 h with magnetic stirring and then was washed by deionized water until the pH reached 7.

Basic Characterization. FE-SEM (Hitachi S-4800) and TEM (JEOL JEM-2100) were used to characterize the morphologies of the samples. The TEM samples were prepared by ultrasonically suspending the powders in ethanol. An FEI Tecnai G2T20 electron microscope was used to obtain TEM and bright-field STEM images. Corresponding EDX mappings were obtained using an FEI Tecnai G2F30 S-TWIN field-emission transmission electron microscope equipped with energy-dispersive X-ray spectroscopy (EDAX) operating at 300 kV. The XRD patterns were recorded with a powder diffractometer (Bruker D8 Advance) using Cu Kα radiation. XPS was carried out using a PHI5000 VersaProbe spectrometer equipped with an Al Kα (1486.6 eV) X-ray source to analyze the surface elemental composition of the samples. The binding energy was calibrated from the C 1s peak at 284.6 eV. A BELSORP II instrument was used to measure the nitrogen adsorption−desorption isotherm of the sample at the boiling point of liquid nitrogen (77 K). The amount of graphene in the composite sample was determined via the thermogravimetric analysis (TGA) with a NETZSCH STA 449 F3 apparatus in air with a heating rate of 10 °C min⁻¹.

Electrochemical Measurement. *Lithium Storage Properties.* Electrochemical measurements were carried out using coin cells. The as-synthesized Fe₃O₄/G material (80 wt %) was prepared as an electrode by mixing with 10 wt % conductive Super P and 10 wt % polyvinylidene fluoride (PVDF) binder in *N*-methylpyrrolidinone (NMP) to obtain a slurry and then coating the slurry onto a copper foil. The mass loading of active material was typically 0.55−0.75 mg cm⁻². Metallic lithium foil and microporous polypropylene film (Celgard, 2400) were used as the counter electrode and separator, respectively. The electrolyte used was a 1 M LiPF₆ solution in a 1:1 (v/v) ethylene carbonate and dimethyl carbonate mixture. Cyclic voltammetry tests were performed between 3.0 and 0.01 V at room temperature using a Princeton Applied Research potentiostat/galvanostat model 273A at a sweep rate of 0.1 mV s⁻¹. The galvanostatic charge/discharge measurements were carried out over the potential range of 0.01−3.0 V using a NEWARE BTS computer-controlled galvanostat (Shenzhen, China) at room temperature.

Catalytic Properties for ORR and OER. All electrochemical measurements were performed using the same mass of catalyst (∼0.2 mg cm⁻²). Linear sweep voltammograms (LSV) were recorded using a glassy-carbon rotating-disk electrode (RDE, 0.196 cm², Pine Research Instrumentation, USA) with a scan rate of 5 mV s⁻¹ or a rotating ring-disk electrode (RRDE, 0.283 cm², Pine Research Instrumentation) with a scan rate of 2 mV s⁻¹. The data were recorded using a CHI 760 D potentiostat (CH Instruments, Inc., USA). The reference electrode was Ag/AgCl in 4 M KCl solution (all potentials were referenced to RHE), and the counter electrode was platinum wire. Electrolyte was O₂-satuated 0.1 M KOH solution (pH 13).

Kinetic Current. The kinetic current for ORR occurring on the electrode can be calculated from the intercept of Koutecky−Levich plot using the following equation:

$$1/j_D = 1/j_K + 1/B\omega^{1/2} \qquad (1)$$

where j_K is the kinetic current density at a constant potential, j_D is the measured current density on RDE, ω is the electrode rotating speed in rpm, and B, the reciprocal of the slope, could be determined from the slope of Koutecky−Levich plot using the Levich equation

$$B = 0.2nFv^{-1/6}C_{O_2}D_{O_2}^{2/3} \qquad (2)$$

where n is the number of electrons transferred per oxygen molecule, F is the Faraday constant (96 485 C mol^{-1}), D_{O_2} is the diffusion coefficient of O_2 in 0.1 M KOH (1.9×10^{-5} cm s^{-1}), v is the kinetic viscosity (0.01013 cm^2 s^{-1}), and C_{O_2} is the concentration of O_2 (1.2×10^{-3} mol L^{-1}). The constant 0.2 is adopted when the rotating speed is in rpm.

Electron Transfer Numbers. The overall electron transfer numbers per oxygen molecule involved in a typical ORR process were determined on the basis of RRDE voltammograms recorded using a RRDE configuration with a 320 μm gap Pt-ring electrode. The disk electrode was scanned cathodically at a rate of 2 mV s^{-1}, and the ring potential was constant at +0.5 V for oxidizing any HO_2^- intermediate. The electron transfer number (n) and HO_2^- intermediate production percentage (%HO_2^-, which serves as 2e$^-$ pathway selectivity) were determined as follows:

$$n = 4 \times \frac{I_d}{I_d + I_r/N} \tag{3}$$

$$\%HO_2^- = 200 \times \frac{I_r/N}{I_d + I_r/N} \tag{4}$$

where I_d is the disk current, I_r is the ring current, and N is the current collection efficiency of the Pt ring, which was determined to be 0.37.

■ ASSOCIATED CONTENT

Ⓢ Supporting Information

Additional information and figures. The Supporting Information is available free of charge on the ACS Publications website at DOI: 10.1021/acsami.5b03477.

■ AUTHOR INFORMATION

Corresponding Authors
*E-mail: meilin.liu@mse.gatech.edu.
*E-mail: shaozp@njtech.edu.cn.

Present Address
B.Z.: School of Materials Science and Engineering, Center for Innovative Fuel Cell and Battery Technologies, Georgia Institute of Technology, Atlanta, GA 30332-0245, USA.

Notes
The authors declare no competing financial interest.

■ ACKNOWLEDGMENTS

■ REFERENCES

(1) Niederberger, M.; Pinna, N. *Metal Oxide Nanoparticles in Organic Solvents: Synthesis, Formation, Assembly and Application*; Springer: New York, 2009.

(2) Arico, A. S.; Bruce, P.; Scrosati, B.; Tarascon, J. M.; Van Schalkwijk, W. Nanostructured Materials for Advanced Energy Conversion and Storage Devices. *Nat. Mater.* **2005**, *4*, 366−377.

(3) Hu, R.; Sun, W.; Chen, Y.; Zeng, M.; Zhu, M. Silicon/Graphene Based Nanocomposite Anode: Large-Scale Production and Stable High Capacity for Lithium Ion Batteries. *J. Mater. Chem. A* **2014**, *2*, 9118−9125.

(4) Zhao, B.; Yang, G.; Ran, R.; Kwak, C.; Jung, D. W.; Park, H. J.; Shao, Z. Facile Synthesis of Porous MgO-CaO-SnOₓ Nanocubes Implanted Firmly on In Situ Formed Carbon Paper and Their Lithium Storage Properties. *J. Mater. Chem. A* **2014**, *2*, 9126−9133.

(5) Schmid, G. *Nanoparticles: From Theory to Application*; Wiley-VCH: Weinheim, Germany, 2010.

(6) Goesmann, H.; Feldmann, C. Nanoparticulate Functional Materials. *Angew. Chem., Int. Ed.* **2010**, *49*, 1362−1395.

(7) Zhang, L.; Wu, H. B.; Lou, X. W. Iron-Oxide-Based Advanced Anode Materials for Lithium Ion Batteries. *Adv. Energy Mater.* **2014**, *4*, 1300958.

(8) Zhu, J.; Yin, Z.; Yang, D.; Sun, T.; Yu, H.; Hoster, H. E.; Hng, H. H.; Zhang, H.; Yan, Q. Hierarchical Hollow Spheres Composed of Ultrathin Fe_2O_3 Nanosheets for Lithium Storage and Photocatalytic Water Oxidation. *Energy Environ. Sci.* **2013**, *6*, 987−993.

(9) Lee, S. H.; Yu, S.-H.; Lee, J. E.; Jin, A.; Lee, D. J.; Lee, N.; Jo, H.; Shin, K.; Ahn, T.-Y.; Kim, Y.-W.; Choe, H.; Sung, Y.-E.; Hyeon, T. Self-Assembled Fe_3O_4 Nanoparticle Clusters as High-Performance Anodes for Lithium Ion Batteries via Geometric Confinement. *Nano Lett.* **2013**, *13*, 4249−4256.

(10) He, C.; Wu, S.; Zhao, N.; Shi, C.; Liu, E.; Li, J. Carbon-Encapsulated Fe_3O_4 Nanoparticles as a High-Rate Lithium Ion Battery Anode Material. *ACS Nano* **2013**, *7*, 4459−4469.

(11) Wu, Y.; Wei, Y.; Wang, J.; Jiang, K.; Fan, S. Conformal Fe_3O_4 Sheath on Aligned Carbon Nanotube Scaffolds as High-Performance Anodes for Lithium Ion Batteries. *Nano Lett.* **2013**, *13*, 818−823.

(12) Jeong, J.-M.; Choi, B. G.; Lee, S. C.; Lee, K. G.; Chang, S.-J.; Han, Y.-K.; Lee, Y. B.; Lee, H. U.; Kwon, S.; Lee, G.; Lee, C.-S.; Huh, Y. S. Hierarchical Hollow Spheres of Fe_2O_3@Polyaniline for Lithium Ion Battery Anodes. *Adv. Mater.* **2013**, *25*, 6250−6255.

(13) Xu, Y.; Jian, G.; Liu, Y.; Zhu, Y.; Zachariah, M. R.; Wang, C. Superior Electrochemical Performance and Structure Evolution of Mesoporous Fe_2O_3 Anodes for Lithium-ion Batteries. *Nano Energy* **2014**, *3*, 26−35.

(14) Wu, Z.-S.; Yang, S.; Sun, Y.; Parvez, K.; Feng, X.; Muellen, K. 3D Nitrogen-Doped Graphene Aerogel-Supported Fe_3O_4 Nanoparticles as Efficient Eletrocatalysts for the Oxygen Reduction Reaction. *J. Am. Chem. Soc.* **2012**, *134*, 9082−9085.

(15) Cummings, C. Y.; Marken, F.; Peter, L. M.; Wijayantha, K. G. U.; Tahir, A. A. New Insights into Water Splitting at Mesoporous α-Fe_2O_3 Films: A Study by Modulated Transmittance and Impedance Spectroscopies. *J. Am. Chem. Soc.* **2012**, *134*, 1228−1234.

(16) Koper, M. T. M. Thermodynamic Theory of Multi-Electron Transfer Reactions: Implications for Electrocatalysis. *J. Electroanal. Chem.* **2011**, *660*, 254−260.

(17) Liang, Y.; Li, Y.; Wang, H.; Zhou, J.; Wang, J.; Regier, T.; Dai, H. Co_3O_4 Nanocrystals on Graphene as a Synergistic Catalyst for Oxygen Reduction Reaction. *Nat. Mater.* **2011**, *10*, 780−786.

(18) Li, Y.; Gong, M.; Liang, Y.; Feng, J.; Kim, J.-E.; Wang, H.; Hong, G.; Zhang, B.; Dai, H. Advanced Zinc-Air Batteries Based on High-Performance Hybrid Electrocatalysts. *Nat. Commun.* **2013**, *4*, 1805.

(19) Maiyalagan, T.; Jarvis, K. A.; Therese, S.; Ferreira, P. J.; Manthiram, A. Spinel-Type Lithium Cobalt Oxide as a Bifunctional Electrocatalyst for the Oxygen Evolution and Oxygen Reduction Reactions. *Nat. Commun.* **2014**, *5*, 3949.

(20) Chen, Y.; Song, B.; Lu, L.; Xue, J. Ultra-Small Fe_3O_4 Nanoparticle Decorated Graphene Nanosheets with Superior Cyclic Performance and Rate Capability. *Nanoscale* **2013**, *5*, 6797−6803.

(21) Wang, R.; Xu, C.; Du, M.; Sun, J.; Gao, L.; Zhang, P.; Yao, H.; Lin, C. Solvothermal-Induced Self-Assembly of Fe_2O_3/GS Aerogels for High Li-Storage and Excellent Stability. *Small* **2014**, *10*, 2260−2269.

(22) Zhang, F.; Zhang, T.; Yang, X.; Zhang, L.; Leng, K.; Huang, Y.; Chen, Y. A High-Performance Supercapacitor-Battery Hybrid Energy Storage Device Based on Graphene-Enhanced Electrode Materials with Ultrahigh Energy Density. *Energy Environ. Sci.* **2013**, *6*, 1623−1632.

(23) Yu, S.-H.; Conte, D. E.; Baek, S.; Lee, D.-C.; Park, S.-K.; Lee, K. J.; Piao, Y.; Sung, Y.-E.; Pinna, N. Structure-Properties Relationship in Iron Oxide-Reduced Graphene Oxide Nanostructures for Li-Ion Batteries. *Adv. Funct. Mater.* **2013**, *23*, 4293−4305.

(24) Zhuo, L.; Wu, Y.; Wang, L.; Ming, J.; Yu, Y.; Zhang, X.; Zhao, F. CO_2-Expanded Ethanol Chemical Synthesis of a Fe_3O_4@Graphene

Composite and Its Good Electrochemical Properties as Anode Material for Li-Ion Batteries. *J. Mater. Chem. A* **2013**, *1*, 3954−3960.

(25) Luo, J.; Liu, J.; Zeng, Z.; Ng, C. F.; Ma, L.; Zhang, H.; Lin, J.; Shen, Z.; Fan, H. J. Three-Dimensional Graphene Foam Supported Fe$_3$O$_4$ Lithium Battery Anodes with Long Cycle Life and High Rate Capability. *Nano Lett.* **2013**, *13*, 6136−6143.

(26) Zhou, Q.; Zhao, Z.; Wang, Z.; Dong, Y.; Wang, X.; Gogotsi, Y.; Qiu, J. Low Temperature Plasma Synthesis of Mesoporous Fe$_3$O$_4$ Nanorods Grafted on Reduced Graphene Oxide for High Performance Lithium Storage. *Nanoscale* **2014**, *6*, 2286−2291.

(27) Sun, Y.; Hu, X.; Luo, W.; Xu, H.; Hu, C.; Huang, Y. Synthesis of Amorphous FeOOH/Reduced Graphene Oxide Composite by Infrared Irradiation and Its Superior Lithium Storage Performance. *ACS Appl. Mater. Interfaces* **2013**, *5*, 10145−10150.

(28) Ye, F.; Zhao, B.; Ran, R.; Shao, Z. Facile Mechanochemical Synthesis of Nano SnO$_2$/Graphene Composite from Coarse Metallic Sn and Graphite Oxide: An Outstanding Anode Material for Lithium-Ion Batteries. *Chem.—Eur. J.* **2014**, *20*, 4055−4063.

(29) Kosova, N.; Devyatkina, E.; Osintsev, D. Dispersed Materials for Rechargeable Lithium Batteries: Reactive and Non-Reactive Grinding. *J. Mater. Sci.* **2004**, *39*, 5031−5036.

(30) Suryanarayana, C. Mechanical Alloying and Milling. *Prog. Mater. Sci.* **2001**, *46*, 1−184.

(31) Li, Y.; Tang, L.; Li, J. Preparation and Electrochemical Performance for Methanol Oxidation of Pt/Graphene Nanocomposites. *Electrochem. Commun.* **2009**, *11*, 846−849.

(32) Li, Y.; Lv, X.; Lu, J.; Li, J. Preparation of SnO$_2$-Nanocrystal/Graphene-Nanosheets Composites and Their Lithium Storage Ability. *J. Phys. Chem. C* **2010**, *114*, 21770−21774.

(33) Moulder, J. F.; Sticlke, W. F.; Sobol, P. E.; Bomben, K. D. *Handbook of X-ray Photoelectron Spectroscopy*; Chastain, J., Ed.; PerkinElmer Corporation: Eden Prairie, MN, 1992.

(34) Park, S.; An, J.; Potts, J. R.; Velamakanni, A.; Murali, S.; Ruoff, R. S. Hydrazine-Reduction of Graphite- and Graphene Oxide. *Carbon* **2011**, *49*, 3019−3023.

(35) Lin, Z.; Yao, Y.; Li, Z.; Liu, Y.; Li, Z.; Wong, C.-P. Solvent-Assisted Thermal Reduction of Graphite Oxide. *J. Phys. Chem. C* **2010**, *114*, 14819−14825.

(36) Wang, T.-Q.; Wang, X.-l.; Lu, Y.; Xiong, Q.-Q.; Zhao, X.-Y.; Cai, J.-B.; Huang, S.; Gu, C.-D.; Tu, J.-P. Self-Assembly of Hierarchical Fe$_3$O$_4$ Microsphere/Graphene Nanosheet Composite: Towards a Promising High-Performance Anode for Li-Ion Batteries. *RSC Adv.* **2014**, *4*, 322−330.

(37) Su, Q.; Xie, D.; Zhang, J.; Du, G.; Xu, B. In Situ Transmission Electron Microscopy Observation of the Conversion Mechanism of Fe$_2$O$_3$/Graphene Anode during Lithiation-Delithiation Processes. *ACS Nano* **2013**, *7*, 9115−9121.

(38) Zhang, M.; Jia, M. High Rate Capability and Long Cycle Stability Fe$_3$O$_4$-Graphene Nanocomposite as Anode Material for Lithium Ion Batteries. *J. Alloys Compd.* **2013**, *551*, 53−60.

(39) Wei, W.; Yang, S.; Zhou, H.; Lieberwirth, I.; Feng, X.; Muellen, K. 3D Graphene Foams Cross-Linked with Pre-Encapsulated Fe$_3$O$_4$ Nanospheres for Enhanced Lithium Storage. *Adv. Mater.* **2013**, *25*, 2909−2914.

(40) Su, Y.; Li, S.; Wu, D.; Zhang, F.; Liang, H.; Gao, P.; Cheng, C.; Feng, X. Two-Dimensional Carbon-Coated Graphene/Metal Oxide Hybrids for Enhanced Lithium Storage. *ACS Nano* **2012**, *6*, 8349−8356.

(41) Zhu, X.; Zhu, Y.; Murali, S.; Stollers, M. D.; Ruoff, R. S. Nanostructured Reduced Graphene Oxide/Fe$_2$O$_3$ Composite As a High-Performance Anode Material for Lithium Ion Batteries. *ACS Nano* **2011**, *5*, 3333−3338.

(42) Zhou, G.; Wang, D.-W.; Li, F.; Zhang, L.; Li, N.; Wu, Z.-S.; Wen, L.; Lu, G. Q.; Cheng, H.-M. Graphene-Wrapped Fe$_3$O$_4$ Anode Material with Improved Reversible Capacity and Cyclic Stability for Lithium Ion Batteries. *Chem. Mater.* **2010**, *22*, 5306−5313.

(43) Cao, X.; Zheng, B.; Rui, X.; Shi, W.; Yan, Q.; Zhang, H. Metal Oxide-Coated Three-Dimensional Graphene Prepared by the Use of Metal-Organic Frameworks as Precursors. *Angew. Chem., Int. Ed.* **2014**, *53*, 1404−1409.

(44) Zhu, X. J.; Wu, W. Y.; Liu, Z.; Li, L.; Hu, J.; Dai, H. L.; Ding, L.; Zhou, K.; Wang, C. Y.; Song, X. G. A Reduced Graphene Oxide-Nanoporous Magnetic Oxide Iron Hybrid as an Improved Anode Material for Lithium Ion Batteries. *Electrochim. Acta* **2013**, *95*, 24−28.

(45) Gao, M.-R.; Cao, X.; Gao, Q.; Xu, Y.-F.; Zheng, Y.-R.; Jiang, J.; Yu, S.-H. Nitrogen-Doped Graphene Supported CoSe$_2$ Nanobelt Composite Catalyst for Efficient Water Oxidation. *ACS Nano* **2014**, *8*, 3970−3978.

(46) Masa, J.; Xia, W.; Sinev, I.; Zhao, A.; Sun, Z.; Gruetzke, S.; Weide, P.; Muhler, M.; Schuhmann, W. Mn$_x$O$_y$/NC and Co$_x$O$_y$/NC Nanoparticles Embedded in a Nitrogen-Doped Carbon Matrix for High-Performance Bifunctional Oxygen Electrodes. *Angew. Chem., Int. Ed.* **2014**, *53*, 8508−8512.

(47) Wang, J.; Zhou, Y.; Xiong, B.; Zhao, Y.; Huang, X.; Shao, Z. Fast Lithium-Ion Insertion of TiO$_2$ Nanotube and Graphene Composites. *Electrochim. Acta* **2013**, *88*, 847−857.